TABLE OF CONTENTS (TOC)

Elucidation into Thermally Induced Internal Porosity in Zinc Oxide Nanorods

Albertus D. Handoko[1,*], Laura-Lynn Liew[1,2], Ming Lin[1], Gopinathan Sankar[3], Yonghua Du[4], Haibin Su[2], Zhili Dong[2], Gregory K. L. Goh[1,2,*]
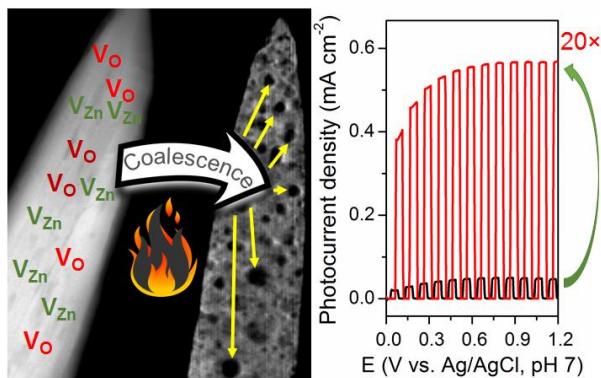
[1] Institute of Materials Research and Engineering, Singapore

[2] Nanyang Technological University, Singapore

[3] University College London, United Kingdom

[4] Institute of Chemical & Engineering Sciences, Singapore

Page Numbers. The font is ArialMT 16 (automatically inserted by the publisher)

The formation of internal porosities in ZnO nanorods tracked using in-situ tomography techniques. 20× higher photocurrent can be obtained as the defect density is lowered and internal pores are formed improving light absorption.

Research Article   **Please choose one**

Elucidation into Thermally Induced Internal Porosity in Zinc Oxide Nanorods

Albertus D. Handoko[1][‡]($\boxtimes$), Laura-Lynn Liew[1,2][‡], Ming Lin[1], Gopinathan Sankar[3], Yonghua Du[4], Haibin Su[2], Zhili Dong[2], Gregory K. L. Goh[1,2]($\boxtimes$)

[1] Agency for Science, Technology and Research (A*STAR), Institute of Materials Research and Engineering, 2 Fusionopolis Way, Innovis, Singapore 138634

[2] Nanyang Technological University, School of Materials Science and Engineering, Blk N4.1 Nanyang Avenue, Singapore 639798

[3] University College London, Department of Chemistry, 20 Gordon St, Kings Cross, London WC1H 0AJ, United Kingdom

[4] Agency for Science, Technology and Research (A*STAR), Institute of Chemical & Engineering Sciences, 1 Pesek Rd, Singapore 627833

[‡] Authors contribute equally

ABSTRACT

In this work, *in situ* electron microscopy, tomography, photoluminescence, and X-ray absorption spectroscopy were utilised to monitor and explain the formation and growth of internal porosity within ZnO nanorods. Careful examination using electron microscopy and tomography indicate that nanosized internal pores start appearing within the individual solution-grown ZnO nanorods upon exposure to heat treatment at 200 °C. The pore volume growth rate was found to be proportional to the heat treatment time, indicating that the process is diffusion controlled, akin to a *reverse* Ostwald ripening-like process. Manageable pore growth rate of $1.4 - 4.4$ nm^3 min^{-1} was observed at 540 °C, suggesting that effective control of internal porosity can be achieved by carefully controlling the heat treatment profile. Mechanistic studies using X-ray absorption spectroscopy indicate that the pore formation is linked to the significant reduction of zinc vacancies after heat treatment. An optimum condition exist where most of the native surface defect is minimised, while the bulk defects are contained within the internal pores. It is also demonstrated that the internal porosity can be exploited to improve the visible light absorption in ZnO. A combination of lower defect density and improved light absorption on heat treated ZnO films thus lead to an increase of more than 20× in the photoelectrochemical response compared to as grown ZnO.

KEYWORDS

_____

Address correspondence to A.D. Handoko, adhandoko@imre.a-star.edu.sg; G.K.L Goh, g-goh@imre.a-star.edu.sg

1. Introduction

Abundant, cheap and naturally *n*-type,[1] ZnO nanorods film is quickly becoming the material of choice for transparent electrodes or electron transport material used in light emitting devices,[2] solar cells[3-5] and wearable devices,[6] as well as anode materials for energy storage.[7, 8] Bulk ZnO is also the leading photocatalyst for water purification as it is more effective and considerably cheaper than TiO_2.[9-11] The ease of obtaining highly crystalline ZnO films or bulk in large quantities at low temperature (90 °C or less) is especially appealing.[12, 13] However, as-grown ZnO is known to be very susceptible to defects, and further treatment like annealing is typically required to bring out the best of its properties.[14, 15]

Recently, it was reported that the annealing process could lead to the formation of internal porosity or external craters in ZnO films and rods.[16-18] While porosities in general is undesirable for optoelectronic applications, porous ZnO have shown promise in niche areas such as battery anode materials,[19] gas sensors,[20] light emitting devices,[21] and catalysis.[22] The formation of internal pores in ZnO has been linked to the expulsion of hydroxyl related defects and subsequent coalescence of zinc (V_{Zn}) and oxygen (V_O) vacancies.[16, 18] However, the porosity growth mechanism, and whether the size and distribution can be controlled are still unclear. A systematic study on the porosity formation during heat treatment would thus provide an invaluable insight to fill the knowledge gap on the porosity formation in ZnO and ultimately gain control and exploit it.

In this work, *in situ* electron microscopy, tomography, photoluminescence, and X-ray absorption spectroscopy were utilised to analyse the formation and growth of porosity within ZnO nanorods. Electron microscopy and tomography revealed the presence of disconnected nanosized pores deep within the ZnO nanorods after heat treatment ≥200 °C. Evidence of Ostwald ripening-like behaviour during the growth of internal porosity in the ZnO nanorods during thermal treatment is observed for the first time using *in situ* high resolution

transmission electron microscope. The pore growth and migration rate was observed to follow a diffusion-controlled rate law when heated at a constant temperature, suggesting that pore size and connectivity may be tuned to the desired size or concentration by modulating the annealing profile. Mechanistic investigations into the porosity formation using X-ray absorption analyses and photoluminescence (PL) measurements demonstrate that the porosity formation is intimately related to the decrease in vacancies after annealing.

More importantly, it is shown that internal porosity in ZnO can be exploited to improve its visible light absorption. A combination of lower defect density and improved light absorption of the heat treated ZnO nanorods films thus lead to more than 20× increase in the photoelectrochemical (PEC) response as compared to the as grown films. Our results highlight that careful control of porosity nucleation and growth in ZnO and other solution-grown materials could open new application fronts such as more sensitive and tunable sensors and highly active photo/electrocatalyts.

2. Results and Discussions

2.1. Porosity growth in ZnO nanorods

The structure of the as-synthesised ZnO nanorod film was ascertained from X-ray diffraction data (Fig 1a). Only diffraction peaks belonging to ZnO (ICSD 52362)[23] or the Si substrate (ICSD 60385)[24] were observed. The strong (002) reflexion seen around 34° 2θ is indicative of a significant *c*-axis texturing in the ZnO film. The *c*-axis texturing seen in XRD was corroborated by electron microscopy, showing that the film is composed of well aligned ZnO nanorods expected from this synthetic route (Fig 1b-c). Cross-sectional view revealed the high aspect ratio of the ZnO nanorods, which vary about 0.9–1.1 μm in length and 50–80 nm in diameter.

It has been reported that thermal annealing of solution grown ZnO could result in the formation of internal porosity.[16, 17] However, very little is known about the formation and growth mechanism
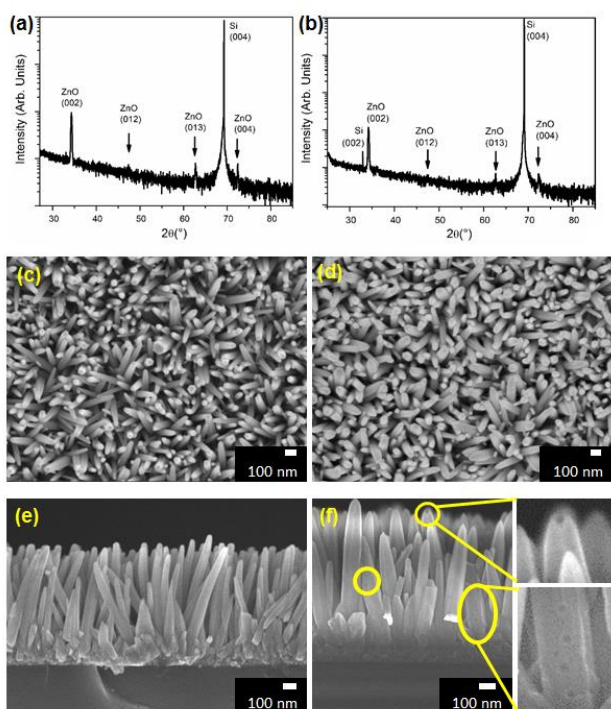
Figure 1: X-ray diffraction data of the (a) as-grown and (b) heat treated ZnO films at 500 °C showing strong (002) texturing after heat treatment. The morphology of the as grown ZnO films consists of well aligned nanorods (c-e). The nanorods morphology was retained after 1 hr heat treatment at 500 °C (d-f), but external craters (yellow circles, insets) started to appear in the cross-sectional view.

of these pores to gain effective control. Systematic *ex situ* annealing of the ZnO nanorods films in air for 1 h at various temperatures between 150–600 °C were then devised to investigate the porosity formation and growth investigation. Only subtle differences could be discerned on the sample surface after heat treatments (Fig 1c-f, ESM Section 1). Most notably, craters start to become visible on the rods exterior after heat treatment at temperatures of 400 °C or higher (Fig 1f, yellow circles, also Fig S1-1 in the ESM). Comparisons between the bright-field TEM micrographs of the as-grown and heat treated samples suggest these craters may have formed in the sub-surface as nanosized (<5 nm) internal pores after heat treatment as low as 200 °C and start to be exposed to the surface from 300 °C onwards (Fig 2, ESM Section 2). It is interesting that larger pores were observed on samples treated at higher temperature, implying an accelerating growth. None of such features was observed on the as-grown samples or

after heat treatment at 150 °C. The electron tomography technique using S/TEM was then used to ascertain that the pores seen in the *bright-field* TEM micrographs exist as internal voids. Electron tomography is a powerful imaging technique that enables 3D visualisation of cells[25] as well as nanostructured crystals.[26, 27] The high angle annular *dark-field* (HAADF) imaging mode used in S/TEM is ideal for this task as it is much more sensitive to mass-thickness contrast, with the intensity roughly proportional to $Z^{1.7}$ (Z being the atomic mass), and not interfered by the complexity associated with diffractions or Fresnel fringes.

Similar pores were observed on the HAADF-S/TEM micrographs on the heat treated sample at different tilt angles (Fig 3b, ZnO heat treated at 500 °C was selected as a representative sample with high density of porosity formation). 3D tomography reconstruction and the corresponding
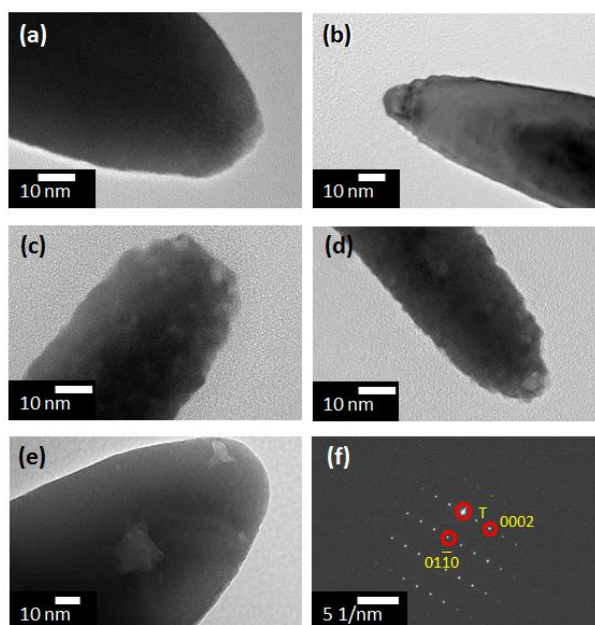

Figure 2: High resolution transmission electron micrograph of individual ZnO rods scraped from ZnO films. No pores were observed on the (a) as grown and after heat treatment at (b) 150 °C. Internal porosities only started to appear after heat treatment at (c) 200 °C and grow upon exposure to higher temperatures: (d) 300 °C, (e) 500 °C. The SAED pattern shown in (f) corresponds to the as-grown rods shown in (a). The diffraction pattern matches the expected pattern from $[\bar{1}2\bar{1}0]$ zone axis of ZnO, and the [0001] direction is parallel to the long axis of the rod. "T" marks the transmitted electron beam spot.

vertical/horizontal slices (Fig 3c-e) the heat treated samples confirm that the pores seen on the bright-field TEM micrographs are actually internal voids sitting deep inside the ZnO nanorods. Such features were absent on the as-grown sample (Fig 3a). The positioning and size distribution of these pores appears to be random without a specific arrangement with respect to the rod's boundary, suggesting that they are not likely to originate from surface reaction with the annealing environment.

Further *in situ* TEM studies were then carried out to find out more about the pore growth process. Temperature dependant observations were first done on a custom made TEM holder capable of controlled heating up to 640 °C. A series of enlarged images are shown in Fig 4 for clarity (full sized images can be found in the ESM Section 3). It was observed that a small number of pores had already formed at the lowest heating power of the hot stage (*approx*. 295 °C, Fig 4a-b). More pores were observed as the temperature was increased and rapid migration and coalescence started occurring above 469 °C (Fig 4c). The growth and migration rate of the pores was found to be faster with increasing temperature; pore coalescence shown in Fig 4d-e (arrows and circles) was completed in less than 10 minutes. As the pore growth rate was too fast during the temperature dependent measurements, an isothermal *in situ* TEM measurement was then devised at a fixed temperature of 540 °C. The isothermal measurement slowed down

the pore growth rate and enabled the tracking of the pore volume (estimated by taking the cube of the pore radius, *r*, see ESM section 4 and 5 for details) and observation of pore movement and coalescence in greater detail.

It was found that the volumes of three selected pores, marked with red, blue and green circles in Fig 5, grew roughly proportional to the heat treatment time during the isothermal *in situ* measurement (ESM section 5). It is thus reasonable to posit that the pore growth occurred through a *reverse* diffusion-limited Ostwald ripening process,[28] where larger pores grow at the expense of smaller ones to minimise the overall surface energy through diffusion. Following the Gibbs-Thomson and Fick's Law,[29] also Lifshitz and Slyozov[30] and Wagner,[31] the rate law in the diffusion-limited Ostwald ripening process can be expressed as:

$$\left(\bar{r}\right)^3 - \left(\bar{r}\right)_0^3 = \frac{8\gamma c_\infty v^2 D}{9 R_g T} t$$

where $\bar{r}$ is the average radius at time t, $\bar{r}_0$ is the average initial radius, γ is the surface energy, c_∞ is the bulk solubility, v is the molar volume, D is diffusion coefficient, R_g is the ideal gas constant and T is the absolute temperature. At a constant temperature, the diffusion coefficient D can be treated as constant, and the pore volume growth should thus be proportional to time.
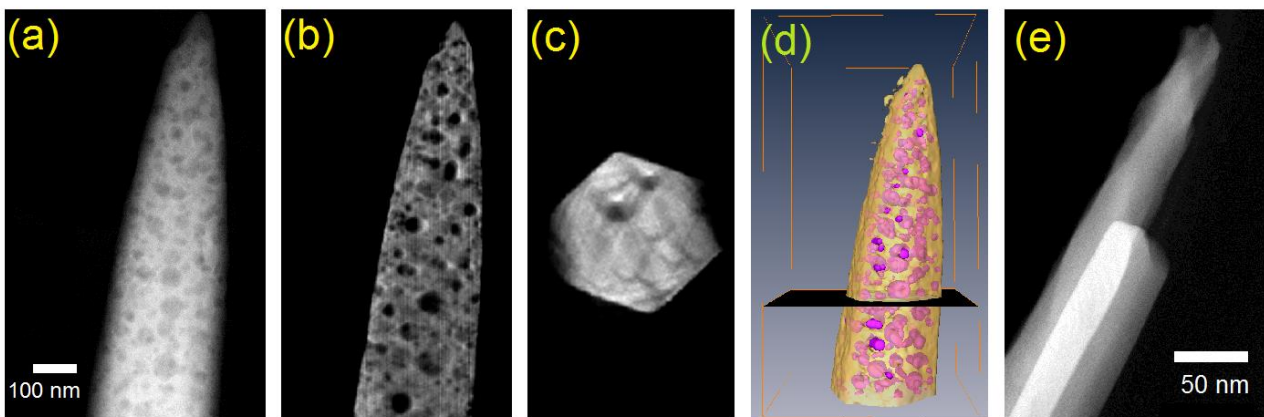

Figure 3: STEM micrographs of ZnO rod (a) after annealing at 500 °C for 1 h in air. (b) Longitudinal and (c) lateral slice-view STEM image showing circular irregularities seen in (d) is actually internally formed pores. (d) 3-D reconstructed tomography micrographs, showing the internal pores within the nanorod at different angles. Black plane indicates the location of lateral slice-view seen in (c). (e) These features were not observed on the as synthesised ZnO rods.

The volumetric growth rate at 540 °C was also observed to be reasonably gentle, from 1.4 to 4.4 nm^3 min^{-1}. This translates to an approximate lateral migration rate of about 1.1–1.6 nm min^{-1}. These measurements indicate that the pore sizes can be effectively controlled by adjusting the heat treatment time.

The slower pore growth rate during the isothermal *in situ* measurement mode also allows us to observe the pore migration, coalescence and annihilation process more clearly. The pore-front migration rate, estimated from the change of distance between pores 2 and 4, was calculated to be about 0.4 nm min^{-1} at this temperature (Fig 5, ESM Section 5). The coalescence of adjacent pores was typically completed within 30-40 minutes (Fig 5 b-e, black arrows). We also observed an interesting pore annihilation behaviour, which starts with the migration of the largest pore towards the surface followed by a radial growth at the expense of the surrounding pores (Fig 5 g-n, white arrows). The annihilation of the surrounding pores within a 12 nm radius took about 240 minutes to complete, accompanied by continual growth and exposures of the inner surface of the largest pore to the nanorod surface. We confirmed that the pore formation was not due to electron beam exposure, and prolonged heat treatment (5 hours) at 540 °C resulted in a visibly shrunk and rough ZnO nanorod (ESM Section 3). Although the defect concentration within the ZnO nanorod is generally expected to be lower after heat treatment process, our finding clearly show that prolonged heat treatment is detrimental to the mechanical and optical properties due to the exposure of the defective periphery of the internal pores to the surface.

2.2. Mechanistic insight into the ZnO structural change after heat treatment

Heat treatment has been often viewed as a *silver bullet* to improve the electronic and optical performance of ZnO, leading to an improved UV (near band-edge, NBE) excitation coupled with reduced defect-level related emission (DLE), and improved photoresponse.[32, 33] While NBE is characteristic to the semiconductor bandgap, DLE describes the wide-band emission at much lower energy level attributed to various defects and imperfections.[34] Lower defect density after heat treatment at modest temperatures is thus cited frequently as the main reason behind the improved performance.[35-37] Curiously, heat treatments at higher temperatures can sometimes be ineffective, or even deleterious to ZnO electro-optical properties.[14, 16, 38] We believe this phenomenon may be related to the dynamics of internal porosity formation and expulsion to the surface, which is the subject of discussion in this section.

Photoluminescence (PL) measurements on ZnO samples treated at different temperatures reveal that the NBE/DLE ratio initially improved with increasing heat treatment up to 300 °C, but deteriorated at higher temperatures (ESM Section 6. We observe that the highest NBE/DLE ratio after 300 °C annealing was a combined effect of a reduced defect-related DLE band and a higher NBE emission. Treatments at >400 °C was found to result in a larger DLE band. Additionally, the centre of the composite DLE bands was found to shift from 590 nm to around 635 nm, suggesting that a different kind of
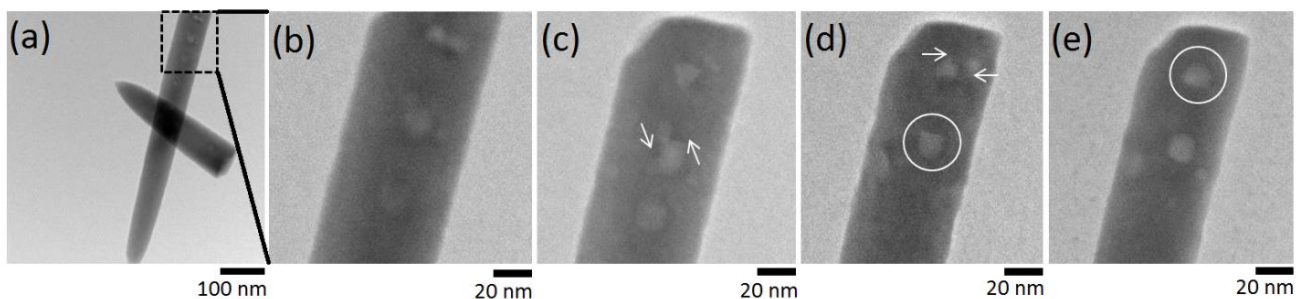

Figure 4: *In-situ* TEM micrograph of ZnO nanorods subjected to heat treatment at increasing temperatures: (a,b) 320 °C, (c) as the temperature reaches 469 °C, (d) as the temperature reaches 553 °C, and (e) finally at 639 °C. White circles showing clear indication of small pores coalescence to form bigger pores as the temperatures increases.

surface defect may have emerged after annealing at higher temperatures. Similar PL profile evolution after heat treatment of ZnO films at different temperatures has been reported previously,[14] and the cause was loosely attributed to the removal of non-radiative defects during annealing.

We turn to X-ray absorption to elucidate the average structural change in the ZnO nanorods film after heat treatment at different temperatures. Refinement of the X-ray absorption fine structure (EXAFS) data revealed significant amount of V_{Zn} on the as-grown ZnO nanorods film (ESM Section 7). This is in line with our previous hypothesis and observation on bulk hydrothermally grown ZnO powders, where incorporated hydroxyls could lead to zinc vacancy formation as charge balance.[16, 39] The average first neighbour (Zn-O) and second neighbour (Zn-Zn) coordination number and the ratio between them quickly becomes closer to the ideal values after heat treatment, indicating that most of the vacancies have been eliminated from the ZnO bulk (Table S7 and Fig S7-3 in the ESM). The ideal ratios were retained even after heat treatment at 600 °C. We note that no significant amounts of vacancy was observed on model ZnO standard obtained from NIST, with both of its Zn-O and Zn-Zn bond length and coordination number remains close to the ideal ratio after heat treatment up to 600 °C, indicating the validity of our refinement strategy.

At a glance, the results from EXAFS measurements appear to contradict the PL data, as the latter suggest that heat treatment only improves the NBE/DLE ratio initially, but worsened once the temperature reaches 400 °C. However it should be noted EXAFS measures the average structural change of the entire bulk while PL measurement is very surface sensitive.[17] A better explanation to the temperature-dependant optical properties of solution-grown ZnO nanorods film may be sought by piecing together evidence obtained from the electron microscopy, PL and EXAFS measurements. The observation of vacancies elimination on the ZnO nanorods film after heat treatment as low as 200 °C is significant, as it provides experimental proof linking the internal pores formation to removal of point defects.[16] As the refined EXAFS data suggest that V_{Zn} and V_O level remain low even after annealing at

400 or 600 °C, the deteriorating PL measurement at such temperature should not be attributed to the bulk defects level, but rather to new surface defects that appears after annealing. Electron microscopy measurement in section 2.1. uncovered significant migration and surface expulsion of internal porosity become more likely after heat treatment at 400 °C or higher (Fig 1-3, ESM Section 2). These newly exposed craters are evidently much more potent than point defect surface migration,[40] exposing large area of disordered surface as it reaches the surface.

Thus in our case, the heat treatment at 300 °C represents an optimum condition where most of the
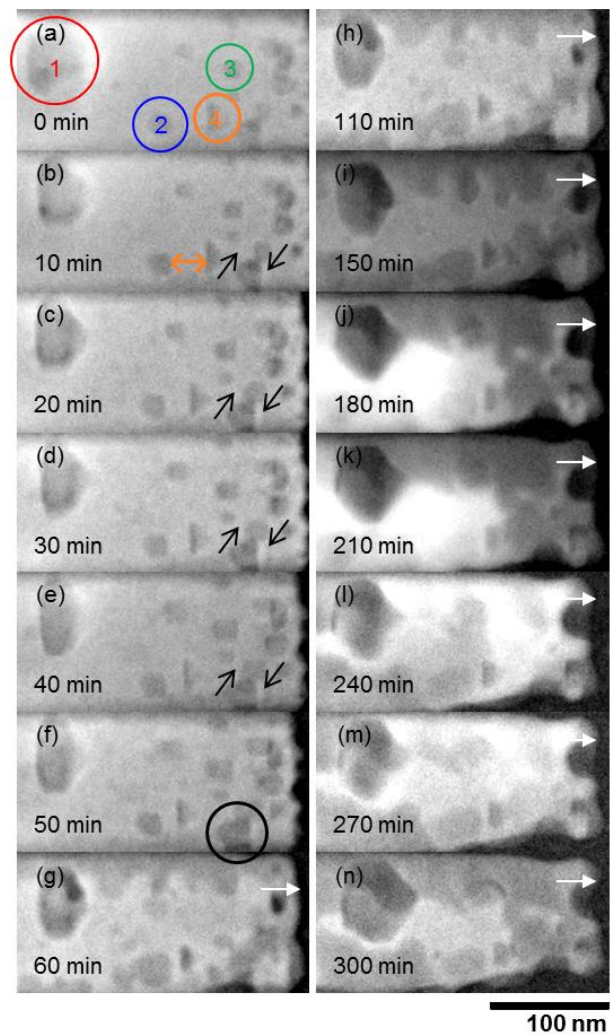

Figure 5: Time resolved micrographs of 250×120 nm section of the ZnO nanorods during in-situ heat treatment inside TEM chamber at a fixed temperature of 540 °C.

native surface defects may have been removed while the bulk defects have been effectively contained on the internal pores. After heat treatment >400 °C, the quenching of NBE emission and emergence of new DLE bands become more likely to occur as defective surfaces were exposed during the pore expulsion process at higher treatment temperature.

2.3. Properties enhancement after optimised heat treatment scheme

Thus far, we have shown that heat treatment could induce the formation and growth of internal porosity in ZnO and alter its photoluminescence and short/medium range structure. In this section we demonstrate that the internal porosity can be exploited to maximise the photoelectrochemical response of undoped ZnO.

It was observed that the ZnO nanorods films become less transparent after heat treatment (ESM Section 8), suggesting that the internal porosity can enhance the diffuse light scattering within the ZnO film, akin to the back reflector of a solar cell.[41] UV-Vis spectroscopy measurements indicate that heat treated samples are 1.6-4.4× more absorbing in the visible light range (between 400 – 700 nm, ESM section 8). We believe the enhanced visible light absorption would be beneficial to wide arrays of applications such as optical sensors or photoelectrodes.
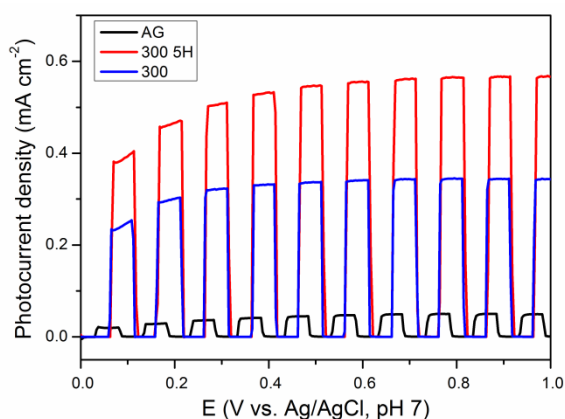

Figure 6: Photocurrent response of the as grown (black trace) and heat treated ZnO at 300 °C for 1 hour (blue trace) and 5 hours (red trace) to chopped simulated solar light (sweep +5 mV/s from 0 to 1.4 V vs. Ag/AgCl, pH 6.8 0.1 M Na_2SO_4). Less than 1.5 $\mu A\,cm^{-2}$ was observed during light-off condition (See ESM Section 9).

PEC measurement was used to evaluate the efficacy of light-induced electron-hole pair generation in the as-grown and heat treated ZnO nanorod film in neutral 0.1 M K_2SO_4 solution. Heat treatment at 300 °C was selected for this test because it had the lowest DLE emission and highest absorption in the visible light range. The PEC response of samples treated at 300 °C clearly shows significantly higher (9×) photocurrent compared to the as-grown ZnO nanorods film (Fig 6). Even better photocurrent response, 14-22× the as-grown ZnO film, could be achieved by heat treating the sample for longer time (5 hrs) at 300 °C (Fig 6, ESM Section 9). We note that the higher photocurrent on the samples subjected to optimum treatment can be sustained for at least 1200 s (ESM Section 9), although degradation due to photocorrosion cannot be avoided as no protection layer was added into the structure. It is significant to point out that the photocurrent response increases significantly despite the lower NBE/DLE emission ratio (ESM Section 6), indicative of higher concentration of non-radiative recombination centres.[42] This phenomenon suggests that the higher light adsorption benefit from the creation or growth of internal pores may have outweighed the downside of increasing non-radiative recombination centres created after longer heat treatment at moderate temperatures.

Larger photocurrent generation have been attributed to a number of factors including higher surface area, improved light absorption, higher crystallinity, or better charge separation due to lower defect density.[43, 44] We can confidently rule out the effect of surface area, as the electroactive surface area was found to be slightly smaller than the as-grown ZnO film (ESM Section 10). The smaller electroactive area can be rationalised by considering that the ZnO nanorods were found to contract significantly after heat treatment (ESM Section 3). Additionally, we did not find any foreign elements on the ZnO nanorods film (ESM Section 11) or significant change in the film crystallinity after heat treatment (ESM Section 12) that could fillip the photo-electrochemical response. The superior photocurrent response should instead be attributed to a combination of lower surface defect density and higher concentration of internal porosities that helps to improve light harvesting and

reduce self-annihilation of the photo-generated electron-hole pair at the same time. We propose that an optimum pore size and distribution may be optimised, where fine tuning of heat treatment period or temperature can alter the size and distribution of internal pores to further increase the ZnO nanorods photoelectrochemical response.

Improved photocurrent response on ZnO has been previously achieved by forming hierarchical structures under extreme deposition control (e.g. ALD),[45] or by adding co-catalysts or photo-sensitisers (PbS, C_3N_4, Pd, ZnS, CdS, CdTe, *etc*.) to the ZnO surface.[46-50] Our work demonstrate that the tendency of ZnO to form internal porosity in itself after heat treatment can be exploited to improve its light absorbing properties and deliver comparable or better photocurrent response than the sensitised or co-catalysed ZnO, removing the need for the expensive growth methods or adding heavy metals or other hazardous substances as co-catalysts. We believe this phenomenon of porosity formation may be extendable to other solution grown oxides, thus increasing the applicability of solution grown films for sensing or catalysis.

3. Conclusions

In this work, the formation, growth, and migration of internal porosity in solution grown ZnO nanorods were systematically tracked for the first time using 3D electron tomography, *in situ* electron microscopy, photoluminescence, and X-ray absorption spectroscopy. It was discovered that pores form instantaneously upon annealing above 200 °C. More pores were nucleated and grow rapidly as the temperature increases. However, the pore growth rate became roughly proportional to heat treatment time when subject to isothermal treatment, suggesting that the pore growth profile is akin to a *reverse* Ostwald ripening where larger pores grow in expense of the smaller ones. Manageable pore volume growth and migration rate of 1.4-4.4 nm^3 min^{-1} also indicate that the size and distribution of these pores can be controlled by tuning the heat treatment profile at moderate temperature around 500 °C.

X-ray absorption analyses suggest that, unlike model ZnO NIST standard, solution grown ZnO

nanorods film contain significant amount of zinc vacancies. The formation of the internal pores within the nanorod was highly correlated with the annihilation of V_{Zn}, affirming the previous hypothesis of that vacancies can indeed coalesce into pores. Through *in-situ* electron microscopy measurements we also show that these pores can, with increased treatment temperature or time, migrate to the surface and expose the defective periphery of the internal pores to the surface, leading to degraded optical and electrical performance of ZnO.

More importantly we show that the internal porosity within ZnO rods can be exploited to improve its light absorption properties. Combined with lower defect density obtained after an optimised heat treatment profile at 300 °C for 5 hrs, the photocurrent response of undoped ZnO can reach similar levels of sensitised or co-catalysed ZnO. We envision that the knowledge of voids creation, migration and agglomeration behaviour will not only provide invaluable insight to improve the compatibility of solution grown ZnO in mainstream device processing, but also provide effective control of these voids and ultimately the ZnO properties can be tailored for specific applications.

4. Experimental

4.1. Sample preparation:

ZnO nanorods films were grown using a two-step solution process reported previously.[51] First, ZnO seeds were grown on 15×15×0.625 mm <100> Si wafer substrate (Latech Scientific Supply) by dripping solution containing zinc acetate dihydrate (>98.0%, Fluka, Sigma-Aldrich Chemie GmbH) and ethanol (absolute, VWR BDH Prolabo). The solution was left on the Si wafer substrate for about 30 s before being rinsed in ethanol and dried with a flow of N_2 gas. This step is repeated five times followed by a thermal decomposition process at 350 °C for 20 mins. The entire cycle was repeated twice to ensure even coverage of the ZnO seeds on the Si wafer.

Subsequent growth of ZnO nanorods films were done in 25 mL aqueous solution containing 0.028 M zinc nitrate hexahydrate (98%, Sigma Aldrich) and 0.028 M of hexamethyltetramine (HMT, 99+%, Alfa Aesar). The ZnO-seeded Si wafer substrate was suspended face down the solution in a Teflon-lined

stainless steel autoclave (Parr 4744). The autoclave was then placed in a calibrated convection oven for 3 hours at 90 °C. Afterwards the films were taken out, rinsed with deionised water and dried with N_2 gas. Individual ZnO rods for microscopic studies were obtained by mechanically scraping the film and dispersing it into ethanol using an ultrasonicator. A few drops of this suspension was then dripped onto TEM grids for further characterisation. For light absorption and photoelectrochemical (PEC) measurements, ZnO films were grown using the same procedure onto cleaned 15×15×1 mm ITO-coated borosilicate glass (15 Ω square^{-1}, Kintec Co.).

4.2. Annealing

Ex situ annealing of the ZnO films was done in air in an alumina crucible placed in a calibrated box furnace. Annealing was done at various temperatures ranging from 150 to 600 °C for 1-5 hours (see main text for details) with a heating rate of 10 °C min^{-1}.

4.3. Characterisation

The overview of ZnO nanorods morphology was first examined using a field emission scanning electron microscope (FESEM, JEOL JSM7600F). X-ray diffraction (XRD) patterns of the films were obtained on a general area detector diffraction system (Bruker D8 Discover GADDS) equipped with double pinhole collimator and high resolution thin film XRD (Panalytical X'pert Pro) equipped with a 4-crystal Ge(220)/(440) monochromator. A transmission electron microscope (TEM, JEOL 2100) was used for obtaining high resolution bright field TEM micrographs as well as selected area electron diffraction data of as grown and *ex situ* annealed ZnO nanorods. Chemical analyses using electron energy loss spectroscopy (EELS, Gatan Tridiem ER) and energy dispersive X-ray spectroscopy (Oxford X-MAX50 EDS) did not detect any foreign metallic elements (ESM Section 1).

X-ray absorption spectroscopy fine structure (XAFS) measurement on ZnO films were done at the XAFCA beamline of the Singapore Synchrotron Light Source (SSLS).[52] In a typical experiment, 15×15 mm^2 portion of the samples grown on Si was mounted onto a Zn-free sample holder, and XAS data was collected in fluorescence mode using a high rate silicon drift detector (Bruker XFlash Detector 6|100). As a comparison, model ZnO standard obtained from NIST (part of the SRM 647b package) was also treated the same way as the ZnO film samples and measured in transmission mode using IC spec ionisation chamber (FMB Oxford). Prior to measurements, Zn^0 edge was calibrated to 9658.6 eV using Zn metal foil.[53] Data treatment was done using Visual Processing in EXAFS Research (VIPER)[54] and ATHENA software package[55] for normalisation and background subtraction. Analysis of the EXAFS data was then performed using ARTEMIS software package[55] and EXCURV98[56] to refine the atomic information. Details on the EXAFS data treatment strategy and analyses are presented in the ESM Section 2.

Electron tomography observations of *ex situ* annealed ZnO nanorods on carbon coated Cu TEM grid (300 mesh, SPI supplies) were carried out using a scanning transmission electron microscope (S/TEM, FEI Titan 80-300, 200 kV) in the high angle annular dark field-scanning transmission electron microscope (HAADF-STEM) mode.

Strategies to obtain high quality STEM tomography have been reported previously.[27, 57] In brief, a total of 75 HAADF-STEM micrographs were collected over a tilt range of -74° to 74° with 2° tilt step, forming the 2D skeleton for electron tomographic reconstruction. Stage tilting and image acquisition were performed automatically by the Xplore-3D tomography program (FEI), while tracking and refocusing of the specimen were carried out manually to shorten the acquisition time. The images were recorded at a magnification of 44,000× on a 1024×1024 pixel image size, corresponding to a resolution of 3.09 nm per pixel. The acquisition time for each image was 20 s. Final tilt series was aligned using a cross-correlation method and reconstructed by the simultaneous iterative reconstruction technique (SIRT).[58] 40 SIRT were performed using Inspect3D software (FEI). Finally, the reconstructed 3D volumetric image was visualised using Amira 4.1 software (FEI).

In situ thermal annealing of ZnO nanorods was carried out inside the JEOL 2000 TEM using a custom made TEM hot-stage with temperature control up to

640 °C. For this purpose, molybdenum TEM grids coated with a layer of silicon oxide membrane (300 mesh, SPI Supplies) was used to avoid chemical reaction between ZnO and the support during the heating process. The structural and morphological evolution of a single ZnO nanorod was tracked during the annealing process. A series of bright field micrographs were obtained at different temperatures and periods. To minimize high energy electron damage to the ZnO nanorods, the electron beam was focused on the samples only during image acquisition and moved away immediately. Treatment of *in situ* bright field image and particle tracking is done using ImageJ 1.51i.[59] Detailed information of the porosity tracking method can be found in the ESM Section 3.

Photoluminescence (PL) measurements were performed at room temperature using a rapid photoluminescence mapping setup (Accent, RPM2000), equipped with CCD detector and He–Cd laser source with excitation wavelength of 325 nm. Scans were performed from 300 to 1000 nm wavelength in 0.5 nm step and 1 second per step scan rate. Each presented spectra is an average of three scans.

The light absorption and transmittance behaviour of the ZnO films were investigated using UV-Vis spectrophotometer (UV-3101PC, Shimadzu) from 200 to 800 nm in 0.5 nm steps at 200 nm min^{-1} scan speed. Photo-electrochemical response was measured in a custom-built acrylic cell with a sealed quartz window. Linear scanning voltammetry (LSV) sweep from 0 to 1.4 V vs. Ag/AgCl reference electrode (3.5 M KCl, Sigma) was performed using Biologic VSP300 potentiostat in aqueous 0.1 M Na_2SO_4 electrolyte (99%, Sigma Aldrich, pH $\approx$6.8) at 5 mV s^{-1} scan rate. A Pt foil ($\approx$2 cm^2, 99.99%, Aldrich) was used as a counter electrode. The reference electrode was calibrated against reversible hydrogen electrode (Hydroflex, Gaskatel GmBH). Ohmic drop was measured using the current interrupt method and hardware compensated (at 80% level) throughout the LSV scan. 150 W solar simulator (Newport 96000) fitted with an AM 1.5 G filter was used to simulate the solar irradiation. The light was manually shuttered at low frequency to simulate alternating light off and light on conditions. Relative external surface areas of ZnO films were estimated using double layer capacitance measurement method. This is done by performing cyclic voltammetry (CV) scans from -0.1 to 0.1 V vs. Ag/AgCl at six different scanning rates between 10 and 60 mV s^{-1} in 0.1 M Na_2SO_4 electrolyte (99%, Sigma Aldrich).[60] The surface area of a blank ITO substrate was also measured as a smooth surface reference with its relative surface roughness set as 1.

References

[1]   Janotti, A. and C.G. Van de Walle, Native point defects in ZnO. *Phys. Rev. B*, **2007**. 76(16): p. 165202.

[2]   Huang, C.-Y., C.-C. Yang, H.-C. Yu, and Y.-C. Chen, Impact of preparation condition of ZnO electron transport layer on performance of hybrid organic-inorganic light-emitting diodes. *J. Appl. Phys.*, **2014**. 115(8): p. 083109.

[3]   Li, S., P. Zhang, Y. Wang, H. Sarvari, D. Liu, J. Wu, Y. Yang, Z. Wang, and Z.D. Chen, Interface engineering of high efficiency perovskite solar cells based on ZnO nanorods using atomic layer deposition. *Nano Res.*, **2017**. 10(3): p. 1092-1103.

[4]   Li, S., P. Zhang, H. Chen, Y. Wang, D. Liu, J. Wu, H. Sarvari, and Z.D. Chen, Mesoporous PbI2

assisted growth of large perovskite grains for efficient perovskite solar cells based on ZnO nanorods. *J. Power Sources*, **2017**. 342: p. 990-997.

[5] Zhang, P., J. Wu, Y. Wang, H. Sarvari, D. Liu, Z.D. Chen, and S. Li, Enhanced efficiency and environmental stability of planar perovskite solar cells by suppressing photocatalytic decomposition. *J. Mater. Chem. A*, **2017**. 5(33): p. 17368-17378.

[6] Moon, T., G.S. Shin, and B. Park, Recent advances in the transparent conducting ZnO for thin-film Si solar cells. *Electron Mater. Lett.*, **2015**. 11(6): p. 917-930.

[7] Shen, X., D. Mu, S. Chen, B. Wu, and F. Wu, Enhanced Electrochemical Performance of ZnO-Loaded/Porous Carbon Composite as Anode Materials for Lithium Ion Batteries. *ACS Appl. Mater. Interfaces*, **2013**. 5(8): p. 3118-3125.

[8] Ullah, S., F. Ahmed, A. Badshah, A. Ali Altaf, R. Raza, B. Lal, and R. Hussain, Solvothermal Preparation of ZnO Nanorods as Anode Material for Improved Cycle Life Zn/AgO Batteries. *PLOS ONE*, **2013**. 8(10): p. e75999.

[9] Lee, K.M., C.W. Lai, K.S. Ngai, and J.C. Juan, Recent developments of zinc oxide based photocatalyst in water treatment technology: A review. *Water Res.*, **2016**. 88: p. 428-448.

[10] Cheng, C., A. Amini, C. Zhu, Z. Xu, H. Song, and N. Wang, Enhanced photocatalytic performance of TiO_2-ZnO hybrid nanostructures. *Sci Rep*, **2014**. 4: p. 4181.

[11] Tian, C., Q. Zhang, A. Wu, M. Jiang, Z. Liang, B. Jiang, and H. Fu, Cost-effective large-scale synthesis of ZnO photocatalyst with excellent performance for dye photodegradation. *Chem. Commun.*, **2012**. 48(23): p. 2858-2860.

[12] Andeen, D., L. Loeffler, N. Padture, and F.F. Lange, Crystal chemistry of epitaxial ZnO on (1 1 1) $MgAl_2O_4$ produced by hydrothermal synthesis. *J. Cryst. Growth*, **2003**. 259(1-2): p. 103-109.

[13] Byrappa, K., A.S. Dayananda, C.P. Sajan, B. Basavalingu, M.B. Shayan, K. Soga, and M. Yoshimura, Hydrothermal preparation of ZnO:CNT and TiO_2:CNT composites and their photocatalytic applications. *J. Mater. Sci.*, **2008**. 43(7): p. 2348-2355.

[14] Tam, K.H., *et al.*, Defects in ZnO Nanorods Prepared by a Hydrothermal Method. *J. Phys. Chem. B*, **2006**. 110(42): p. 20865-20871.

[15] Wenckstern, H.v., H. Schmidt, M. Grundmann, M.W. Allen, P. Miller, R.J. Reeves, and S.M. Durbin, Defects in hydrothermally grown bulk ZnO. *Appl. Phys. Lett.*, **2007**. 91(2): p. 022913.

[16] Richardson, J.J., G.K.L. Goh, H.Q. Le, L.-L. Liew, F.F. Lange, and S.P. DenBaars, Thermally Induced Pore Formation in Epitaxial ZnO Films Grown from Low Temperature Aqueous Solution. *Cryst. Growth Des.*, **2011**. 11(8): p. 3558-3563.

[17] Al-Nafiey, A., B. Sieber, B. Gelloz, A. Addad, M. Moreau, J. Barjon, M. Girleanu, O. Ersen, and R. Boukherroub, Enhanced Ultraviolet Luminescence of ZnO Nanorods Treated by High-Pressure Water Vapor Annealing (HWA). *J. Phys. Chem C*, **2016**. 120(8): p. 4571-4580.

[18] Pourrahimi, A.M., D. Liu, R.L. Andersson, V. Ström, U.W. Gedde, and R.T. Olsson, Aqueous Synthesis of (2$\bar{1}$0) Oxygen-Terminated Defect-Free Hierarchical ZnO Particles and Their Heat Treatment for Enhanced Reactivity. *Langmuir*, **2016**. 32(42): p. 11002-11013.

[19] Wang, Y., X. Jiang, L. Yang, N. Jia, and Y. Ding, In Situ Synthesis of C/Cu/ZnO Porous Hybrids as Anode Materials for Lithium Ion Batteries. *ACS Appl. Mater. Interfaces*, **2014**. 6(3): p. 1525-1532.

[20] Zhang, J., S. Wang, M. Xu, Y. Wang, B. Zhu, S. Zhang, W. Huang, and S. Wu, Hierarchically Porous ZnO Architectures for Gas Sensor Application. *Cryst. Growth Des.*, **2009**. 9(8): p. 3532-3537.

[21] Mao, P., A.k. Mahapatra, J. Chen, M. Chen, G. Wang, and M. Han, Fabrication of Polystyrene/ZnO Micronano Hierarchical

Structure Applied for Light Extraction of Light-Emitting Devices. *ACS Appl. Mater. Interfaces*, **2015**. 7(34): p. 19179-19188.

[22] Cho, S., J.-W. Jang, J.S. Lee, and K.-H. Lee, Porous ZnO-ZnSe nanocomposites for visible light photocatalysis. *Nanoscale*, **2012**. 4(6): p. 2066-2071.

[23] Fuller, M.L., A Method of Determining the Axial Ratio of a Crystal from X-ray Diffraction Data: The Axial Ratio and Lattice Constants of Zinc Oxide. *Science*, **1929**. 70(1808): p. 196-198.

[24] Wyckoff, R.W.G., *Crystal Structures - Volume 1*. 1963, New York: Interscience Publishers.

[25] Wolf, S.G., L. Houben, and M. Elbaum, Cryo-scanning transmission electron tomography of vitrified cells. *Nat. Methods*, **2014**. 11(4): p. 423-428.

[26] Ding, Y., F. Zhang, and Z. Wang, Deriving the three-dimensional structure of ZnO nanowires/nanobelts by scanning transmission electron microscope tomography. *Nano Res.*, **2013**. 6(4): p. 253-262.

[27] Tan, H.R., J.P.Y. Tan, C. Boothroyd, T.W. Hansen, Y.L. Foo, and M. Lin, Experimental Evidence for Self-Assembly of CeO_2 Particles in Solution: Formation of Single-Crystalline Porous CeO_2 Nanocrystals. *J. Phys. Chem C*, **2011**. 116(1): p. 242-247.

[28] Krost, A., *et al.*, Ostwald ripening and flattening of epitaxial ZnO layers during in situ annealing in metalorganic vapor phase epitaxy. *Appl. Phys. Lett.*, **2004**. 85(9): p. 1496-1498.

[29] Hale, P.S., L.M. Maddox, J.G. Shapter, N.H. Voelcker, M.J. Ford, and E.R. Waclawik, Growth Kinetics and Modeling of ZnO Nanoparticles. *J. Chem. Educ.*, **2005**. 82(5): p. 775.

[30] Lifshitz, I.M. and V.V. Slyozov, The kinetics of precipitation from supersaturated solid solutions. *J. Phys. Chem. Solids*, **1961**. 19(1–2): p. 35-50.

[31] Wagner, C., Theorie der Alterung von Niederschlägen durch Umlösen (Ostwald-Reifung) [Theory of the aging of precipitates by

dissolution-reprecipitation (Ostwald ripening)]. *Zeitschrift für Elektrochemie*, **1961**. 65 (7): p. 581–591.

[32] Deka Boruah, B. and A. Misra, Energy-Efficient Hydrogenated Zinc Oxide Nanoflakes for High-Performance Self-Powered Ultraviolet Photodetector. *ACS Appl. Mater. Interfaces*, **2016**. 8(28): p. 18182-18188.

[33] Vuong, N.M., J.L. Reynolds, E. Conte, and Y.-I. Lee, H:ZnO Nanorod-Based Photoanode Sensitized by CdS and Carbon Quantum Dots for Photoelectrochemical Water Splitting. *J. Phys. Chem C*, **2015**. 119(43): p. 24323-24331.

[34] Rodnyi, P.A. and I.V. Khodyuk, Optical and luminescence properties of zinc oxide (Review). *Opt. Spectrosc.*, **2011**. 111(5): p. 776-785.

[35] Camarda, P., R. Schneider, R. Popescu, L. Vaccaro, F. Messina, G. Buscarino, S. Agnello, F.M. Gelardi, and M. Cannas, Effect of thermal annealing on the luminescence of defective ZnO nanoparticles synthesized by pulsed laser ablation in water. *Phys. Status Solidi C*, **2016**. 13(10-12): p. 890-894.

[36] Wang, Z., S. Su, F.C.-C. Ling, W. Anwand, and A. Wagner, Thermal evolution of defects in undoped zinc oxide grown by pulsed laser deposition. *J. Appl. Phys.*, **2014**. 116(3): p. 033508.

[37] Ridhuan, N.S., K. Abdul Razak, Z. Lockman, and A. Abdul Aziz, Structural and Morphology of ZnO Nanorods Synthesized Using ZnO Seeded Growth Hydrothermal Method and Its Properties as UV Sensing. *PLoS ONE*, **2012**. 7(11): p. e50405.

[38] Pourrahimi, A.M., D. Liu, V. Strom, M.S. Hedenqvist, R.T. Olsson, and U.W. Gedde, Heat treatment of ZnO nanoparticles: new methods to achieve high-purity nanoparticles for high-voltage applications. *J. Mater. Chem. A*, **2015**. 3(33): p. 17190-17200.

[39] Liew, L.-L., G. Sankar, A.D. Handoko, G.K.L. Goh, and S. Kohara, Understanding the defect

structure of solution grown zinc oxide. *J. Solid State Chem.*, **2012**. 189: p. 63-67.

[40] Wang, Y., O. Warschkow, and L.D. Marks, Surface evolution of rutile TiO_2 (100) in an oxidizing environment. *Surf Sci.*, **2007**. 601(1): p. 63-67.

[41] Tsao, Y.-C., T. Søndergaard, E. Skovsen, L. Gurevich, K. Pedersen, and T.G. Pedersen, Pore size dependence of diffuse light scattering from anodized aluminum solar cell backside reflectors. *Opt. Express*, **2013**. 21(S1): p. A84-A95.

[42] Yalishev, V.S., S.U. Yuldashev, K.T. Igamberdiev, T.W. Kang, and B.H. Park, Near-band-edge photoluminescence from ZnO film: Negative thermal quenching and role of adsorbed oxygen. *Journal of the Korean Physical Society*, **2014**. 64(1): p. 1-5.

[43] Pastor, E., *et al.*, Interfacial charge separation in Cu_2O/RuO_x as a visible light driven CO_2 reduction catalyst. *Phys. Chem. Chem. Phys.*, **2014**. 16(13): p. 5922-5926.

[44] Ho-Kimura, S., S.J.A. Moniz, A.D. Handoko, and J. Tang, Enhanced photoelectrochemical water splitting by nanostructured $BiVO_4$-TiO_2 composite electrodes. *J. Mater. Chem. A*, **2014**. 2(11): p. 3948-3953.

[45] Bang, S., S. Lee, Y. Ko, J. Park, S. Shin, H. Seo, and H. Jeon, Photocurrent detection of chemically tuned hierarchical ZnO nanostructures grown on seed layers formed by atomic layer deposition. *Nanoscale Res. Lett.*, **2012**. 7(1): p. 290.

[46] Li, X., J. Li, C. Cui, Z. Liu, and Y. Niu, PbS Nanoparticle Sensitized ZnO Nanowire Arrays to Enhance Photocurrent for Water Splitting. *J. Phys. Chem C*, **2016**. 120(8): p. 4183-4188.

[47] Wang, Y., R. Shi, J. Lin, and Y. Zhu, Enhancement of photocurrent and photocatalytic activity of ZnO hybridized with graphite-like C_3N_4. *Energy Environ Sci.*, **2011**. 4(8): p. 2922-2929.

[48] Ashok, B. and B. Durga, Pd-nanoparticle-decorated ZnO nanowires: ultraviolet photosensitivity and photoluminescence properties. *Nanotechnology*, **2011**. 22(26): p. 265501.

[49] Bera, A. and D. Basak, Photoluminescence and Photoconductivity of ZnS-Coated ZnO Nanowires. *ACS Appl. Mater. Interfaces*, **2010**. 2(2): p. 408-412.

[50] Wang, X., H. Zhu, Y. Xu, H. Wang, Y. Tao, S. Hark, X. Xiao, and Q. Li, Aligned ZnO/CdTe Core−Shell Nanocable Arrays on Indium Tin Oxide: Synthesis and Photoelectrochemical Properties. *ACS Nano*, **2010**. 4(6): p. 3302-3308.

[51] Greene, L.E., M. Law, J. Goldberger, F. Kim, J.C. Johnson, Y. Zhang, R.J. Saykally, and P. Yang, Low-Temperature Wafer-Scale Production of ZnO Nanowire Arrays. *Angew. Chem. Int. Ed.*, **2003**. 42(26): p. 3031-3034.

[52] Du, Y., Y. Zhu, S. Xi, P. Yang, H.O. Moser, M.B.H. Breese, and A. Borgna, XAFCA: a new XAFS beamline for catalysis research. *J. Synchrotron Rad.*, **2015**. 22(3): p. 839-843.

[53] Bearden, J.A. and A.F. Burr, Reevaluation of X-Ray Atomic Energy Levels. *Rev. Mod. Phys.*, **1967**. 39(1): p. 125-142.

[54] Klementev, K.V., Deconvolution problems in x-ray absorption fine structure spectroscopy. *J. Phys. D: Appl. Phys.*, **2001**. 34(15): p. 2241.

[55] Ravel, B. and M. Newville, ATHENA, ARTEMIS, HEPHAESTUS: data analysis for X-ray absorption spectroscopy using IFEFFIT. *J. Synchrotron Rad.*, **2005**. 12(4): p. 537-541.

[56] Binsted, N., *EXCURV98*, in *CCLRC Daresbury Laboratory computer program*. 1998: Daresbury, Chesire. p. CCLRC Daresbury Laboratory computer program.

[57] Tan, J.P.Y., H.R. Tan, C. Boothroyd, Y.L. Foo, C.B. He, and M. Lin, Three-Dimensional Structure of CeO_2 Nanocrystals. *J. Phys. Chem C*, **2011**. 115(9): p. 3544-3551.

[58] Lin, M., H.R. Tan, J.P.Y. Tan, C. Boothroyd, Y.L. Foo, and C.B. He, Transmission Electron Microscope Tomography of Nanostructured

Materials. *J. Nanoeng. Nanomanuf.*, **2011**. 1(3): p. 257-264.

[59]   Rasband, W., *ImageJ*. 2016, National Institute of Health: Maryland, USA. p. Image Processing and Analysis in Java.

[60]   Handoko, A.D.*, et al.*, Enhanced activity of H_2O_2-treated copper(ii) oxide nanostructures for the electrochemical evolution of oxygen. *Catal. Sci. Tech.*, **2016**. 6(1): p. 269-274.